Research Square

Preprints are preliminary reports that have not undergone peer review.
They should not be considered conclusive, used to inform clinical practice,
or referenced by the media as validated information.

Physics-Based Stochastic Mapping of Wear–Corrosion Synergy and Metal-Ion Release in Ti-6Al-4V, CoCrMo and 316L Biomedical Alloys: A Coupled Contact-Mechanics and Depassivation–Repassivation Framework

sudharsan M

sudharsan.m@presidencyuniversity.in

Presidency University

K Prakash

Presidency University

Research Article

Keywords: Tribocorrosion, wear–corrosion synergy, depassivation, repassivation, biomedical alloys, Ti-6Al-4V, CoCrMo, 316L stainless steel, mechanism maps, Sobol sensitivity analysis, Monte Carlo uncertainty, fretting corrosion, modular taper.

Posted Date: November 25th, 2026

DOI: https://doi.org/10.21203/rs.3.rs-11574395/v1

License: This work is licensed under a Creative Commons Attribution 4.0 International License.
Read Full License

Additional Declarations: No competing interests reported.

Physics-Based Stochastic Mapping of Wear–Corrosion Synergy and Metal-Ion Release in Ti-6Al-4V, CoCrMo and 316L Biomedical Alloys: A Coupled Contact-Mechanics and Depassivation–Repassivation Framework

Sudharsan M and K Prakash

Abstract

Tribocorrosion of passive implant alloys is usually quantified after the fact, by splitting a measured material loss into pure wear, pure corrosion and their synergy following ASTM G119. This bookkeeping does not tell an implant designer how the synergy will change with load, sliding speed, electrode potential, protein content or surface treatment, nor how uncertain that prediction is. We present TriboSyn, a physics-based framework that couples Hertzian contact mechanics with wear-induced track widening, Archard wear with Langmuir protein boundary lubrication, asperity-swept depassivation with saturation, exponential repassivation kinetics with a potential-dependent film charge, Faraday conversion, third-body enhancement of mechanical wear and a galvanic mixed-potential model of the open-circuit potential (OCP). The framework is solved by an adaptive ordinary-differential-equation (ODE) integrator and by a vectorized closed form that reproduces the ODE solution with a mean absolute error of 1.37%; a pass-resolved simulation of the moving contact confirms the averaged current within 0.29% at physiological sliding frequency. Applied to Ti-6Al-4V, CoCrMo and 316L stainless steel sliding against alumina in phosphate-buffered saline (10 N, 1 Hz, 1 h, $+0.2$ V vs Ag/AgCl), the model predicts total losses of 54.9, 14.7 and 72.1×10^{-3} mm^3 with synergy fractions of 42.2%, 78.2% and 77.3%, and OCP drops of 572, 229 and 191 mV. Potential–velocity mechanism maps show that the corrosion–wear boundary ($\Psi = 1$) lies at $+0.51$ V for Ti-6Al-4V but at -0.26 and -0.18 V for CoCrMo and 316L. Variance-based Sobol analysis attributes 54% of the variance in dissolved metal to the repassivation pair (i_{pk}, τ), and Monte Carlo propagation gives 90% intervals that span roughly one order of magnitude. A surface-engineering design map and an OCP-coupled fretting model of a ceramic-head modular taper show that metal release at the taper is limited by cathodic capacity rather than by micromotion amplitude. The framework is intended for calibration against new experiments.

Index Terms

Tribocorrosion, wear–corrosion synergy, depassivation, repassivation, biomedical alloys, Ti-6Al-4V, CoCrMo, 316L stainless steel, mechanism maps, Sobol sensitivity analysis, Monte Carlo uncertainty, fretting corrosion, modular taper.

I. Introduction

METALLIC implants survive in the body because a nanometre-thin passive oxide separates a reactive metal from a chloride-rich, protein-laden electrolyte [1]–[4]. When two surfaces slide, fret or are abraded, that film is removed locally, the bare metal dissolves at current densities several orders of magnitude above the passive value, and the film regrows within milliseconds to tens of milliseconds [5]–[7]. Wear and corrosion therefore do not simply add. Mechanical action accelerates dissolution, dissolution products act as third bodies that accelerate wear, and the combined loss can exceed the sum of the separate losses several-fold [5], [8], [9]. This interaction, tribocorrosion, governs debris and metal-ion release at hip and knee bearings, at modular taper junctions and at

Sudharsan M (corresponding author) and K Prakash are with Presidency University, Bengaluru, Karnataka, India (e-mail: sudharsan.m@presidencyuniversity.in; prakashk@presidencyuniversity.in).

The ORCID iDs of Sudharsan M and K Prakash are 0000-0002-0528-3076 and 0000-0003-4073-5207, respectively.

The authors received no specific funding for this research from any funding agency in the public, commercial, or not-for-profit sectors.

dental implant connections [10]–[15]. The same physics limits the life of offshore, tidal and process components [16]–[18].

Experimental practice has converged on electrochemically controlled tribometers and on the ASTM G119 decomposition of the total loss T into pure wear W_0, pure corrosion C_0, corrosion-enhanced wear ΔW_c and wear-enhanced corrosion ΔC_w [8], [9], [19]. That decomposition is diagnostic: it describes one test condition. A designer who wants to know how a femoral stem, a taper or a coated dental abutment will behave at another load, frequency, potential or protein concentration has to repeat the test matrix, and the scatter between nominally identical tests is often a large fraction of the mean [7], [19]. Mechanistic models of the Mischler–Landolt school [6], [7], [20]–[24] and of the Stack mapping school [25], [26] have explained many of the trends. However, they are normally applied one mechanism at a time, deterministically, and without a quantified statement of which inputs control the prediction.

This paper closes that gap with a single framework, TriboSyn, that is predictive across operating space and honest about uncertainty. The contributions are as follows.

1) A coupled model that links Hertzian contact with wear-induced track widening, protein-modulated Archard wear, saturating asperity depassivation, potential- and frequency-dependent repassivation charge, Faraday conversion, third-body wear and the ASTM G119 decomposition, all in one set of equations (Section III).
2) A galvanic mixed-potential extension that predicts the OCP during sliding and couples the anodic worn area to a finite cathodic capacity, which is essential at crevice-like taper junctions (Section III-H).
3) Verification of the time-averaged current against a pass-resolved simulation of the moving contact, with an explicit validity limit in terms of τ/t_ℓ, and of the closed form against an adaptive ODE solution (Section IV).
4) Potential–velocity mechanism maps, variance-based (Sobol) global sensitivity analysis, Monte Carlo uncertainty propagation and a surface-engineering design map for three clinically used alloys (Section V).
5) An OCP-coupled fretting projection for a ceramic-head modular taper showing that metal release is capped by cathodic capacity (Section V-J).

The study is computational. Every parameter is a representative value within published ranges, and every result is labelled as a model prediction. The intent is to provide a calibrated-ready predictive tool and a set of testable hypotheses, not to replace tribocorrosion experiments.

II. Related Work

A. Electrochemical Methods and Synergy Bookkeeping

Landolt, Mischler and Stemp critically appraised potentiostatic, potentiodynamic and OCP measurements during sliding and showed how each technique weights anodic and cathodic areas differently [6]. Landolt reviewed the electrochemical and materials aspects of tribocorrosion systems [5], and Watson *et al.* formalised the measurement of synergism that underlies ASTM G119 [8], [9]. López-Ortega *et al.* reviewed the test procedures and the remaining gaps in standardisation [19]. Mischler compared triboelectrochemical techniques and interpretation methods and introduced a mechanistic estimate of wear-accelerated corrosion from the depassivated area and the repassivation charge [7].

B. Mechanistic Tribocorrosion Models

Jemmely *et al.* modelled passivation transients in tribocorrosion [20], and Landolt *et al.* added material fluxes and third bodies [21]. Papageorgiou and Mischler simulated the coupled current–potential response of a sliding contact with distributed electrochemistry [24]. Cao *et al.* extended the approach to mixed lubrication in metal-on-metal hip joints [22] and reviewed the field [23]. von der Ohe *et al.* combined static and cyclic loading of passive metals in seawater [16]. For fretting, Mace and Gilbert assessed an asperity-based electrochemical and micro-mechanical model for CoCrMo, Ti-6Al-4V and 316L [27], and Swaminathan and Gilbert characterised CoCrMo/Ti-6Al-4V interfaces [28]. Barril *et al.* mapped the effect of fretting regime on Ti-6Al-4V [29].

C. Mapping

Lim and Ashby introduced wear-mechanism maps for dry sliding [26]. Stack and co-workers transferred the concept to aqueous wear–corrosion, using the ratio of corrosion to wear contributions to define wear-dominated, wear–corrosion, corrosion–wear and corrosion-dominated regimes [25]. Such maps are usually built from sparse experiments or from separately fitted laws.

D. Biomedical Context

Clinical retrievals and studies of modular hip prostheses have documented mechanically assisted crevice corrosion [11]–[13]. Laboratory work on CoCrMo has shown the importance of carbon content, biofilms, proteins and tribochemical layers [30]–[36]. Ti-6Al-4V shows strong sensitivity to protein and fluoride [15], [37], [38], a central issue in implant dentistry [39], and additively manufactured 316L differs from wrought material [40]. Surface treatments such as thermal oxidation, anodising and TiO_2 nanotubes are used to raise hardness and reduce depassivation [17], [41], [42].

E. Gap

Table I positions this work. To our knowledge, no published framework combines contact evolution, saturation of the depassivated area, potential- and frequency-dependent repassivation charge, protein effects, an OCP model, ASTM G119 decomposition, global sensitivity analysis and uncertainty propagation for several implant alloys in one reproducible code base.

TABLE I
CAPABILITIES OF REPRESENTATIVE TRIBOCORROSION MODELS

Feature	[7]	[24]	[22]	[25]	[27]	This work
Contact evolution $w(t)$	–	–	✓	–	–	✓
Repassivation kinetics	✓	✓	✓	–	✓	✓
Potential dependence	–	✓	–	✓	✓	✓
OCP / galvanic coupling	–	✓	–	–	✓	✓
G119 decomposition	✓	–	–	✓	–	✓
Protein effect	–	–	✓	–	–	✓
Mechanism maps	–	–	–	✓	–	✓
Global sensitivity	–	–	–	–	–	✓
Uncertainty propagation	–	–	–	–	–	✓
Several alloys	–	–	–	–	✓	✓

III. MATERIALS AND METHODS: THE TRIBOSYN MODEL

Fig. 1 summarises the configuration and the information flow. A flat alloy specimen slides against an alumina ball of radius $R = 3$ mm in a reciprocating motion of stroke $L = 5$ mm and frequency f, under normal load F_n, in phosphate-buffered saline (PBS) with optional bovine serum albumin (BSA) of concentration c_{alb}. The potential E is either imposed (potentiostatic mode) or free (OCP mode). All potentials are referred to Ag/AgCl (saturated KCl).

A. Contact Mechanics and Track Evolution

The effective modulus of the alloy–alumina pair and the Hertzian contact radius and peak pressure are [43]

$$\frac{1}{E^*} = \frac{1-\nu_1^2}{E_1} + \frac{1-\nu_2^2}{E_2}, \tag{1}$$

$$a = \left(\frac{3F_n R}{4E^*}\right)^{1/3}, \qquad p_0 = \frac{3F_n}{2\pi a^2}. \tag{2}$$

Wear converts the initially elastic contact into a conformal groove. For a spherical slider, the groove of width w and length L has volume $V \simeq Lw^3/(12R)$, so the track width follows from the cumulative mechanical loss $V_m(t)$:

$$w(t) = \max\left[2a,\ \left(\frac{12R\,V_m(t)}{L}\right)^{1/3}\right]. \tag{3}$$

Equation (3) is the feedback loop in Fig. 1(b). A wider track lowers the mean pressure and enlarges the area that can be depassivated.

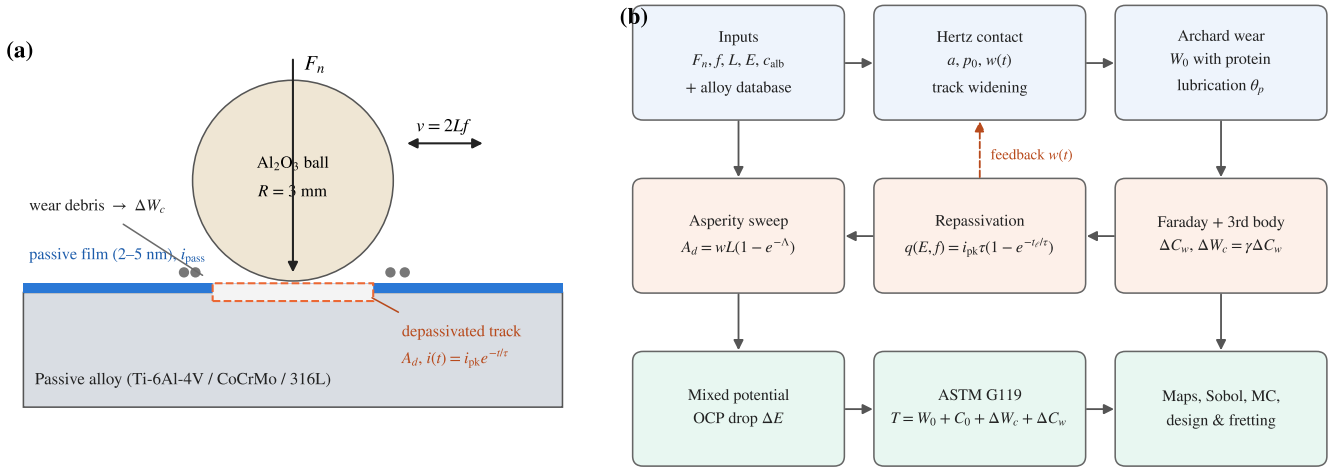

Fig. 1. TriboSyn framework. (a) Ball-on-flat configuration: the counterbody removes the passive film over the depassivated area A_d, which repassivates with transient current $i(t)$; oxide debris acts as a third body. (b) Information flow between the model blocks. The dashed arrow marks the feedback of track width $w(t)$ on contact pressure and depassivated area.

B. Mechanical Wear with Protein Lubrication

Pure mechanical wear follows Archard's law [44] with a dimensionless coefficient K_m and hardness H:

$$\dot{V}_{m,0} = \frac{K_m F_n v}{H}, \qquad v = 2Lf. \tag{4}$$

Adsorbed albumin acts as a boundary lubricant. We describe its surface coverage with a Langmuir isotherm and let it reduce the wear coefficient:

$$\theta_p = \frac{K_{\text{ads}} c_{\text{alb}}}{1 + K_{\text{ads}} c_{\text{alb}}}, \tag{5}$$

$$K_m = K_0 \left(1 - \eta_w \theta_p\right), \tag{6}$$

with $K_{\text{ads}} = 0.2$ L g^{-1} and an alloy-specific efficiency η_w.

C. Depassivated Area

Within the apparent track, the counterbody touches the alloy only at asperities. The real contact area is $A_r = F_n/H$. If the contacting asperities have a characteristic radius r_a, each pass of length L sweeps a depassivated area $2LA_r/(\pi r_a)$. That area cannot exceed the track area wL, so we write the saturating form

$$A_d = wL\left[1 - \exp(-\Lambda)\right], \qquad \Lambda = \frac{2F_n}{\pi H r_a w}. \tag{7}$$

For $\Lambda \ll 1$ (wide tracks, light loads), $A_d \to 2LF_n/(\pi H r_a)$ and is proportional to the load. For $\Lambda \gg 1$, the whole track is bare after each pass.

D. Repassivation Charge

After depassivation, the bare surface carries an anodic transient that decays as the film regrows,

$$i(t) = i_{\text{pk}}\, e^{-t/\tau} + i_{\text{pass}}, \tag{8}$$

where i_{pk} is the peak bare-metal current density, τ the repassivation time constant and i_{pass} the passive current density [7], [20]. In reciprocating sliding, a point on the track is passed twice per cycle, so the latency time between passes is $t_\ell = 1/(2f)$. The charge passed per unit area between successive passes is

$$q_0(f) = \int_0^{t_\ell} i_{\text{pk}} e^{-t/\tau}\, dt = i_{\text{pk}}\, \tau \left[1 - e^{-t_\ell/\tau}\right]. \tag{9}$$

The regrown film thickness, and hence the charge, increases with the overpotential above the passivation potential E_{pp} (high-field growth). Albumin may inhibit or enhance dissolution [32], [33]; we capture both with a signed coefficient η_c:

$$q(E, f, c_{\mathrm{alb}}) = q_0(f)\,\left\langle \frac{E - E_{\mathrm{pp}}}{E_{\mathrm{ref}} - E_{\mathrm{pp}}} \right\rangle (1 - \eta_c \theta_p), \tag{10}$$

where $\langle x \rangle = \max(x, 0)$ and $E_{\mathrm{ref}} = +0.2$ V is the potential at which i_{pk} is specified.

E. Wear-Accelerated Corrosion and Third-Body Wear

The anodic current during sliding is the sum of the depassivation term and the passive current on the track:

$$I(t) = 2f\, A_d(t)\, q(E, f, c_{\mathrm{alb}}) + i_{\mathrm{pass}}\, w(t) L. \tag{11}$$

Faraday's law converts charge to volume through the alloy equivalent weight,

$$\frac{M}{n} = \left(\sum_j \frac{x_j n_j}{M_j} \right)^{-1}, \qquad \dot{V}_c = \frac{I(t)}{F\rho}\,\frac{M}{n}, \tag{12}$$

where x_j, n_j and M_j are the mass fraction, valence and molar mass of element j, F is Faraday's constant and ρ the density. Oxide debris generated by wear-accelerated corrosion is trapped in the contact and abrades the surface [21]. We represent this corrosion-enhanced wear as proportional to the wear-accelerated corrosion rate,

$$\dot{V}_{wc} = \gamma \left(\dot{V}_c - \dot{V}_{c,0} \right), \tag{13}$$

with third-body factor γ and $\dot{V}_{c,0} = i_{\mathrm{pass}} w L M/(nF\rho)$.

F. Governing System and ASTM G119 Decomposition

The state vector $\mathbf{y} = [V_{m,0}, V_c, V_{c,0}, V_{wc}]^{\mathsf{T}}$ obeys

$$\frac{d\mathbf{y}}{dt} = \left[\dot{V}_{m,0},\ \dot{V}_c,\ \dot{V}_{c,0},\ \dot{V}_{wc} \right]^{\mathsf{T}} \big(V_m = V_{m,0} + V_{wc} \big), \tag{14}$$

which is non-linear through (3) and (7). At the end of a test of duration t_e, the ASTM G119 terms are

$$W_0 = V_{m,0}(t_e), \qquad C_0 = \frac{i_{\mathrm{pass}}\, 2aL\, t_e}{F\rho}\,\frac{M}{n}, \tag{15}$$

$$\Delta C_w = V_c(t_e) - C_0, \qquad \Delta W_c = V_{wc}(t_e), \tag{16}$$

$$T = W_0 + C_0 + \Delta W_c + \Delta C_w, \qquad S = \Delta W_c + \Delta C_w. \tag{17}$$

We report the synergy fraction S/T, the synergism factor $T/(W_0 + C_0)$, the dissolved metal mass $m_{\mathrm{ion}} = \rho V_c(t_e)$, and the corrosion-attribution ratio

$$\Psi = \frac{T - W_0}{W_0} = \frac{C_0 + \Delta C_w + \Delta W_c}{W_0}, \tag{18}$$

which compares all corrosion-attributable loss with pure mechanical wear. Following Stack [25], we classify the regime as wear dominated ($\Psi < 0.1$), wear–corrosion ($0.1 \le \Psi < 1$), corrosion–wear ($1 \le \Psi < 10$) or corrosion dominated ($\Psi \ge 10$). We use Ψ instead of the ratio $(C_0 + \Delta C_w)/(W_0 + \Delta W_c)$. Under (13), the latter ratio is bounded by $1/\gamma$, so it cannot reach the corrosion–wear regime whatever the electrochemistry.

G. Closed-Form Approximation

For maps, sensitivity analysis and Monte Carlo sampling, which require 10^5 evaluations, we use a vectorised closed form. Because $V_m \propto t$ at near-constant K_m, (3) gives $w \propto t^{1/3}$ once wear dominates the width, and the time-averaged width is $\langle w \rangle = \frac{3}{4} w(t_e)$. Then

$$V_{\mathrm{wac}} = 2f\, A_d(\langle w \rangle)\, q\, t_e\, \frac{M}{nF\rho}, \tag{19}$$

$$V_m^{(k+1)} = W_0 + \gamma V_{\mathrm{wac}}\big(w(V_m^{(k)}) \big), \tag{20}$$

iterated three times from $V_m^{(0)} = W_0$. Section IV quantifies the error.

H. Open-Circuit Potential During Sliding

At OCP, the anodic current of the worn and passive areas must equal the cathodic (oxygen-reduction) current on the passive area $A_s - wL$ of the specimen. We describe the cathode with Tafel kinetics in series with a diffusion limit,

$$i_c(E) = \left[\frac{1}{i_{\mathrm{pass}} 10^{-(E - E_{\mathrm{rest}})/b_c}} + \frac{1}{i_{\mathrm{lim}}} \right]^{-1}, \tag{21}$$

with $b_c = 0.12$ V dec^{-1}, $i_{\mathrm{lim}} = 3$ μA cm^{-2} and $A_s = 1$ cm^2. The sliding OCP E_{mix} is the root of

$$2 f A_d \, q(E_{\mathrm{mix}}, f) + i_{\mathrm{pass}} A_s = i_c(E_{\mathrm{mix}}) \, (A_s - wL), \tag{22}$$

found by Brent's method. Because q in (10) decreases as $E \to E_{\mathrm{pp}}$, (22) produces a self-limiting OCP drop, which is the behaviour observed in OCP tribocorrosion tests [6], [24].

I. Pass-Resolved Reference Simulation

To test the averaging behind (11), we discretise the depassivated band into N_{cell} cells along the stroke. A cell is reset when the contact centre crosses it, at time $t_{\ell,j}$, and then contributes $\Delta A \, i_0 \, e^{-(t - t_{\ell,j})/\tau}$, where i_0 is chosen so that a uniform latency reproduces (9). The contact follows a triangular stroke, so cells near the reversal points are revisited after unequal intervals, which the averaged model ignores. The current is integrated exactly over each time step $\Delta t \le \min(\tau/8,\, 1/(4000 f))$.

J. Global Sensitivity and Uncertainty Quantification

For the output $Y = g(\mathbf{X})$ of d independent inputs, the first-order and total-order Sobol indices are [45], [46]

$$S_i = \frac{\mathrm{Var}_{X_i}\big[\mathbb{E}(Y|X_i)\big]}{\mathrm{Var}(Y)}, \quad S_{T,i} = \frac{\mathbb{E}_{\mathbf{X}_{\sim i}}\big[\mathrm{Var}(Y|\mathbf{X}_{\sim i})\big]}{\mathrm{Var}(Y)}. \tag{23}$$

With two independent sample matrices $\mathbf{A}, \mathbf{B}$ and $\mathbf{A}_B^{(i)}$ ($\mathbf{A}$ with column i from $\mathbf{B}$), we use the Saltelli and Jansen estimators [46]:

$$\hat{S}_i = \frac{1}{N \hat{V}} \sum_{k=1}^{N} g(\mathbf{B}_k) \big[g(\mathbf{A}_{B,k}^{(i)}) - g(\mathbf{A}_k) \big], \tag{24}$$

$$\hat{S}_{T,i} = \frac{1}{2 N \hat{V}} \sum_{k=1}^{N} \big[g(\mathbf{A}_k) - g(\mathbf{A}_{B,k}^{(i)}) \big]^2. \tag{25}$$

We draw $N = 8192$ scrambled Sobol' points in $2d = 20$ dimensions ($N(d+2) = 98\,304$ model runs) and obtain 95% confidence intervals from 200 bootstrap resamples. The ten inputs and ranges (Ti-6Al-4V) are $K_0 \in [1, 6] \times 10^{-4}$, $H \in [3.0, 3.8]$ GPa, $i_{\mathrm{pk}} \in [0.5, 5]$ A cm^{-2}, $\tau \in [1, 10]$ ms, $r_a \in [3, 30]$ μm (log-uniform for these five apart from H), $\gamma \in [0.5, 3]$, $F_n \in [2, 20]$ N, $f \in [0.5, 2]$ Hz, $E \in [-0.2, 0.6]$ V and $c_{\mathrm{alb}} \in [0, 40]$ g L^{-1}. The outputs are $\log_{10} T$ and $\log_{10} m_{\mathrm{ion}}$.

For uncertainty propagation at the reference condition, each uncertain material parameter is a log-normal multiplier with unit mean,

$$X = \bar{X} \exp(\xi), \quad \xi \sim \mathcal{N}\Big(-\tfrac{s^2}{2}, s^2\Big), \quad s^2 = \ln(1 + \mathrm{CV}^2), \tag{26}$$

with coefficients of variation 0.5 (K_0, r_a), 0.4 (i_{pk}, τ), 0.3 (γ) and 0.1 (H), and 2×10^4 samples per alloy.

K. Fretting at a Modular Taper

For small-amplitude oscillation of amplitude δ, each asperity micro-contact of radius a_r carries load $P_c = H\pi a_r^2$ and enters gross slip above the Mindlin threshold [43]

$$\delta_t = \frac{3\mu P_c}{16 G^* a_r}, \qquad \frac{1}{G^*} = \frac{2-\nu_1}{G_1} + \frac{2-\nu_2}{G_2}. \tag{27}$$

In partial slip, the slipping annulus occupies the fraction δ/δ_t of the contact. In gross slip, each half-cycle sweeps $\pi a_r^2 + 4a_r(\delta - \delta_t)$. With $N_c = A_t p_n/(H\pi a_r^2)$ micro-contacts on a taper of nominal area $A_t = 150$ mm^2 and pressure $p_n = 50$ MPa, the depassivated area per half-cycle is

$$A_d^{\mathrm{fr}} = N_c \begin{cases} \pi a_r^2\, \delta/\delta_t, & \delta < \delta_t, \\ \pi a_r^2 + 4a_r(\delta - \delta_t), & \delta \geq \delta_t. \end{cases} \tag{28}$$

The taper potential follows from (22) with a cathodic area $A_{\mathrm{cath}} = 50$ cm^2 (exposed head and stem), $a_r = 5$ μm, $\mu = 0.3$, a gait frequency of 1 Hz and 10^6 cycles. A fixed-potential bound at E_{rest} is computed for comparison.

L. Parameters and Implementation

Table II lists the material parameters. The elastic constants, hardness and density are typical handbook values for wrought or cast implant grades [1]–[4]. The electrochemical parameters are representative of reported repassivation transients and passive currents in saline and serum [7], [20], [30], [32], [33], [37]. The wear coefficients give specific wear rates of 8.8×10^{-5}, 8.9×10^{-6} and 4.5×10^{-5} mm^3 N^{-1} m^{-1} for Ti-6Al-4V, CoCrMo and 316L, in the ranges reported against ceramic counterbodies in saline. The signs of η_c encode the observation that albumin tends to inhibit dissolution of titanium but can enhance dissolution of CoCrMo through complexation [31]–[33]. Note that all values are representative, not fitted, and the Monte Carlo study in Section V-H propagates their uncertainty. Algorithm 1 summarises the computation. The code (Python 3, NumPy, SciPy, Matplotlib) runs every experiment of this paper in 23 s on one CPU core.

TABLE II
MATERIAL AND ELECTROCHEMICAL PARAMETERS (REPRESENTATIVE VALUES; POTENTIALS VS AG/AGCL)

Parameter	Ti-6Al-4V	CoCrMo	316L SS
Elastic modulus E (GPa)	114	210	193
Poisson ratio ν	0.34	0.30	0.30
Hardness H (GPa)	3.4	4.5	2.2
Density ρ (kg m^{-3})	4430	8300	8000
Equivalent weight M/n (g mol^{-1})	11.87	24.02	25.12
Wear coefficient K_0 ($-$)	3.0×10^{-4}	4.0×10^{-5}	1.0×10^{-4}
Peak bare-metal current i_{pk} (A cm^{-2})	2.0	0.6	1.0
Repassivation constant τ (ms)	3	8	10
Passive current i_{pass} (μA cm^{-2})	0.10	0.05	0.20
Passivation potential E_{pp} (V)	-0.70	-0.45	-0.35
Rest OCP E_{rest} (V)	-0.10	-0.20	-0.15
Third-body factor γ ($-$)	1.5	1.0	1.2
Protein wear factor η_w ($-$)	0.30	0.40	0.25
Protein corrosion factor η_c ($-$)	+0.25	-0.25	+0.10

IV. VERIFICATION

Fig. 2(a) compares the pass-resolved current with the averaged current (11) for Ti-6Al-4V at the reference condition. The pass-resolved signal ripples as cells are reset and dips briefly at the stroke reversals, but its mean differs from the averaged value by only 0.29%. The error depends on the ratio τ/t_ℓ [Fig. 2(b)]. It stays below 1.7% for $\tau/t_\ell < 0.05$, which covers all three alloys at $f \leq 1$ Hz, and reaches -12.3% at $\tau/t_\ell \approx 0.62$. In that range, unequal revisit intervals near the stroke ends leave the film incompletely regrown, which the uniform-latency model overestimates. The averaged model should therefore be corrected or replaced by the pass-resolved one for high-frequency fretting of slowly repassivating alloys.

Algorithm 1 TriboSyn evaluation for one operating point

Require: alloy parameters, F_n, f, L, E, c_{alb}, t_e

compute E^*, a, p_0 by (1)–(2); θ_p by (5)
compute $q(E, f, c_{\mathrm{alb}})$ by (9)–(10)
integrate (14) with LSODA ($r_{\mathrm{tol}} = 10^{-8}$), updating w by (3) and A_d by (7) at every call
evaluate W_0, C_0, ΔC_w, ΔW_c, T, S, Ψ, m_{ion} by (15)–(18)
if OCP mode **then** solve (22) for E_{mix} by Brent's method
end if
return decomposition, $I(t)$, $w(t)$, E_{mix}

Fig. 2(c) compares the closed form with the ODE solution for 18 cases (three alloys, $F_n = 1$–40 N). The mean absolute percentage error is 1.37% and the maximum is 3.55%. Table III shows that the ODE result converges monotonically with tolerance; at $r_{\mathrm{tol}} = 10^{-8}$ it is within 5×10^{-7}% of the 10^{-11} reference. The pass-resolved mean converges with cell count to within 0.3% for $N_{\mathrm{cell}} \geq 400$.

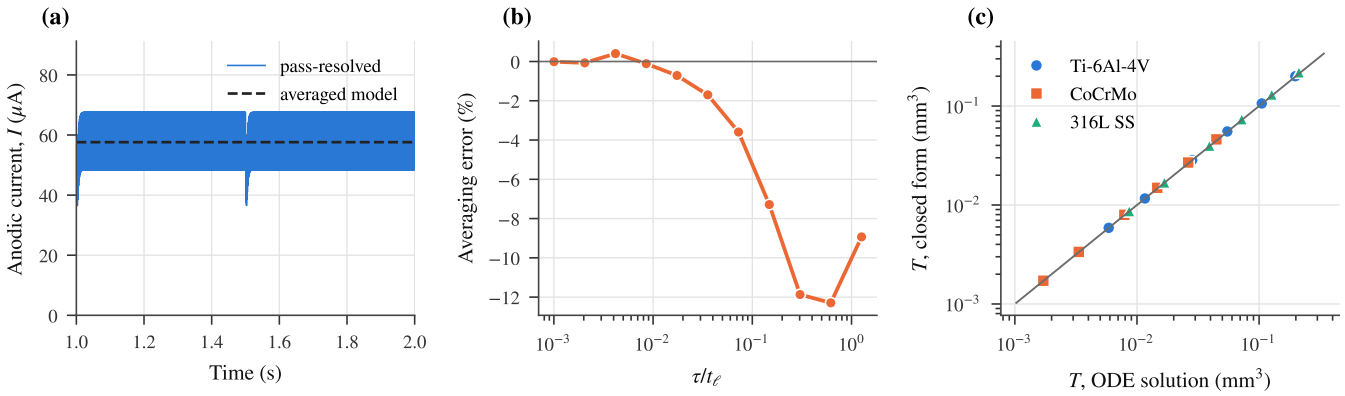

Fig. 2. Verification. (a) Pass-resolved anodic current (one cycle) and the averaged model for Ti-6Al-4V (10 N, 1 Hz, +0.2 V). The fast ripple comes from discrete cell resets; the dip marks a stroke reversal. (b) Error of the averaged current versus τ/t_ℓ. (c) Closed form versus ODE solution of T for three alloys and $F_n = 1$–40 N; the line marks parity.

TABLE III
NUMERICAL CONVERGENCE

(a) ODE tolerance (Ti-6Al-4V, reference case)			
r_{tol}	T (10^{-3} mm^3)	Error (%)	RHS evals
10^{-3}	54.9466	4.03e-03	73
10^{-4}	54.9450	1.12e-03	117
10^{-6}	54.9443	4.19e-05	193
10^{-8}	54.9443	4.55e-07	292
10^{-10}	54.9443	3.64e-09	317
(b) Track discretisation (pass-resolved current)			
N_{cell}	$\bar{I}$ (μA)	Error (%)	
25	58.476	1.496	
50	58.409	1.379	
100	58.208	1.031	
200	58.058	0.770	
400	57.446	0.291	
800	57.444	0.296	

V. Results

Unless stated otherwise, the reference condition is $F_n = 10$ N, $f = 1$ Hz ($v = 10$ mm s^{-1}), $L = 5$ mm, $t_e = 1$ h, $E = +0.2$ V and PBS without protein.

A. Repassivation Kinetics

Fig. 3(a) shows the repassivation transients (8). Ti-6Al-4V has the largest peak current but the shortest time constant (3 ms). 316L has the slowest decay (10 ms), and its passive current is twice that of Ti-6Al-4V. At $f = 1$ Hz, the latency of 500 ms is far longer than every τ, so the charges per event in Fig. 3(b) reach their asymptotes: 6.0, 4.8 and 10.0 mC cm^{-2} for Ti-6Al-4V, CoCrMo and 316L. At 50 Hz, the film has no time to regrow completely, and the charge falls by 3.6%, 28.7% and 36.8%. Slowly repassivating alloys therefore benefit most, per event, from high-frequency motion, although the number of events per second rises in proportion.

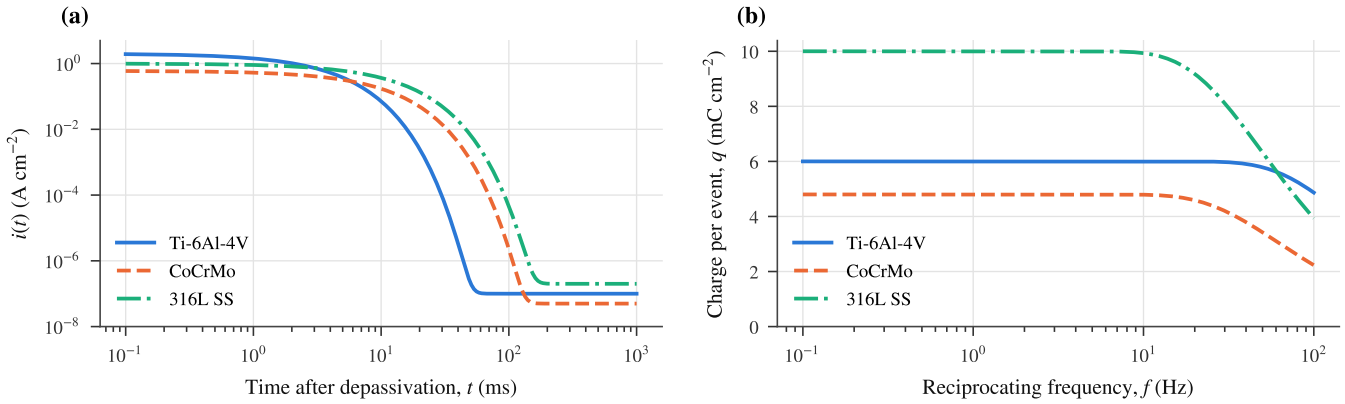

Fig. 3. (a) Repassivation transients after a depassivation event. (b) Charge per depassivation event versus reciprocating frequency at +0.2 V.

B. Time Evolution of a Test

Fig. 4(a) shows that the anodic current is not constant during a test. It rises from 57.6 to 98.4 μA for Ti-6Al-4V, from 37.7 to 57.2 μA for CoCrMo and from 101 to 237 μA for 316L. The rise is caused by track widening [Fig. 4(b)]: the width grows from the Hertzian value $2a$ of 107–123 μm to 690, 401 and 696 μm, which increases the area available for depassivation in (7). The initial Hertzian peak pressures are 1.27, 1.66 and 1.60 GPa, but they fall rapidly as the track conforms. Fig. 4(c) shows the cumulative Ti-6Al-4V loss split into W_0, ΔW_c and the chemical term. All three grow nearly linearly, so a 1-h test is representative of the steady state.

C. Load Dependence and OCP Drop

The potentiostatic current grows with load as $I \propto F_n^{\beta}$ with $\beta = 0.88$, 0.85 and 0.82 over 2–40 N [Fig. 5(a)]. The exponent is below unity because wider tracks at high load dilute the asperity sweep. In OCP mode [Fig. 5(b)], the rest potentials of -0.10, -0.20 and -0.15 V drop during sliding at 10 N to -0.674, -0.430 and -0.345 V, that is by 572, 229 and 191 mV. The drop saturates near E_{pp} because the repassivation charge vanishes there (Eq. (10)) and the cathode is diffusion-limited. The shallower drop of CoCrMo and 316L reflects the smaller potential window between E_{rest} and E_{pp}. A large OCP drop is therefore not, by itself, evidence of a large corrosion rate: Ti-6Al-4V shows the largest drop and the smallest synergy fraction. Fig. 5(c) shows the initial Hertz pressure for reference.

D. Synergy Decomposition

Table IV and Fig. 6(a) give the ASTM G119 decomposition. Pure corrosion C_0 is negligible (below 1.3×10^{-7} mm^3) for all alloys. In PBS, Ti-6Al-4V loses the most by pure wear ($W_0 = 31.8 \times 10^{-3}$ mm^3), but its synergy fraction is only 42.2%. CoCrMo has the smallest total loss (14.7×10^{-3} mm^3), yet 78.2% of it is synergistic,

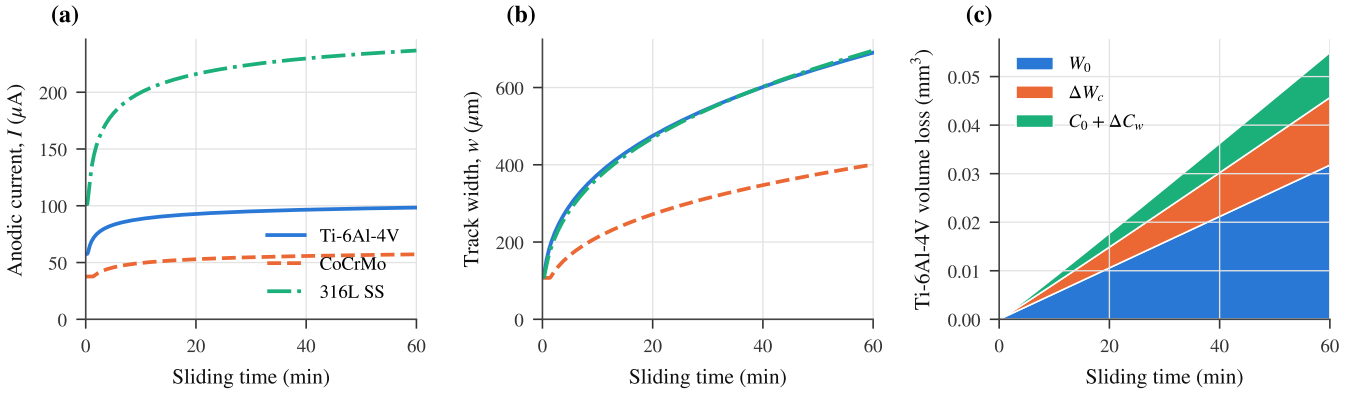

Fig. 4. Reference test (10 N, 1 Hz, +0.2 V, PBS). (a) Anodic current, (b) track width, (c) cumulative Ti-6Al-4V volume loss by component.

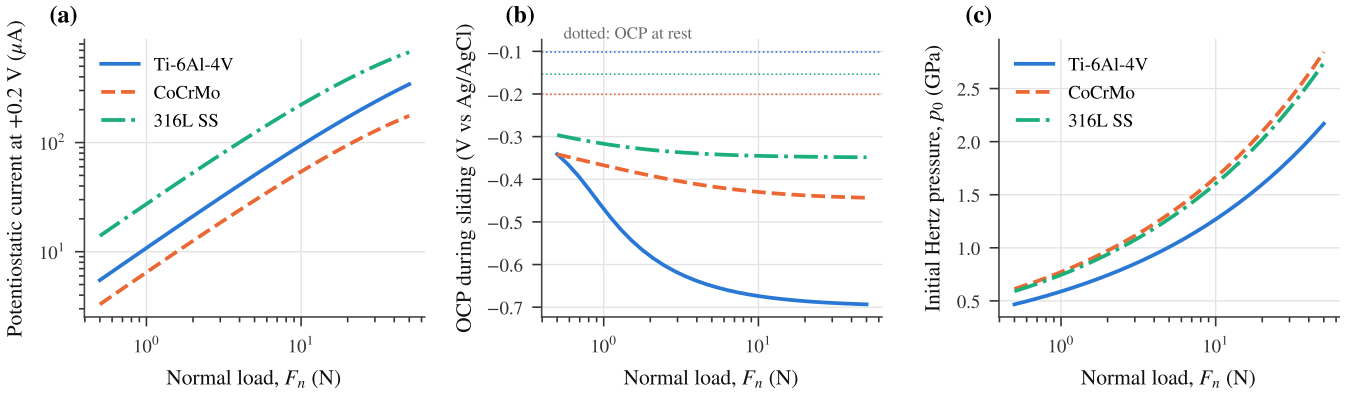

Fig. 5. Load dependence at 1 Hz. (a) Potentiostatic current at +0.2 V after 1 h. (b) OCP during sliding; dotted lines mark the OCP at rest. (c) Initial Hertzian peak pressure.

because its pure wear is ten times smaller while its wear-accelerated corrosion is of the same order. 316L combines moderate wear with the largest repassivation charge and loses 72.1×10^{-3} mm^3, 77.3% of it by synergy. The synergism factors $T/(W_0 + C_0)$ are 1.73, 4.58 and 4.40. For CoCrMo, $\Delta W_c = \Delta C_w$ because $\gamma = 1$.

The dissolved metal mass is 41.1, 47.6 and 202.5 μg per test. In terms of ion release, CoCrMo is therefore not better than Ti-6Al-4V, although its volume loss is a quarter of that of Ti-6Al-4V. This distinction matters biologically, because metal ions and particles provoke different tissue responses [11], [13].

Adding 20 g L^{-1} albumin lowers T by 23% for Ti-6Al-4V and by 12% for 316L, but raises it by 9% for CoCrMo; the CoCrMo ion release rises by 20%. The synergy fraction of CoCrMo increases to 86.3% because albumin lubricates (smaller W_0) while enhancing dissolution (larger ΔC_w). Fig. 6(b) shows that S/T increases monotonically with potential. Between -0.3 and $+0.8$ V it rises from 24.6% to 55.6% for Ti-6Al-4V, from 44.4% to 87.9% for CoCrMo and from 22.6% to 88.4% for 316L.

E. Mechanism Maps

Fig. 7 presents potential–velocity maps of the regime defined by Ψ (18), with iso-lines of S/T. The maps answer a design question directly: at which potential does corrosion-attributable loss exceed pure wear? At 10 mm s^{-1}, the boundary $\Psi = 1$ lies at $+0.51$ V for Ti-6Al-4V, but at -0.26 V for CoCrMo and -0.18 V for 316L. The wear-dominated region ($\Psi < 0.1$) lies below -0.57, -0.43 and -0.33 V, just above the respective E_{pp}. Over the mapped domain, Ti-6Al-4V is in the wear–corrosion regime on 66.5% of the area, whereas CoCrMo and 316L are

TABLE IV
ASTM G119 DECOMPOSITION AT THE REFERENCE CONDITION (10 N, 1 HZ, 5 MM STROKE, 1 H, +0.2 V VS AG/AGCL; ODE SOLUTION). $C_0 < 1.3 \times 10^{-7}$ MM^3 FOR ALL CASES

Alloy	Medium	W_0	ΔW_c (10^{-3} mm^3)	ΔC_w	T	S/T (%)	$T/(W_0{+}C_0)$ (−)	m_{ion} (μg)
Ti-6Al-4V	PBS	31.76	13.91	9.27	54.94	42.2	1.73	41.1
	PBS+20 g/L BSA	24.14	10.94	7.30	42.38	43.0	1.76	32.3
CoCrMo	PBS	3.20	5.73	5.73	14.66	78.2	4.58	47.6
	PBS+20 g/L BSA	2.18	6.88	6.88	15.93	86.3	7.32	57.1
316L SS	PBS	16.36	30.38	25.32	72.06	77.3	4.40	202.5
	PBS+20 g/L BSA	13.09	27.58	22.98	63.66	79.4	4.86	183.9

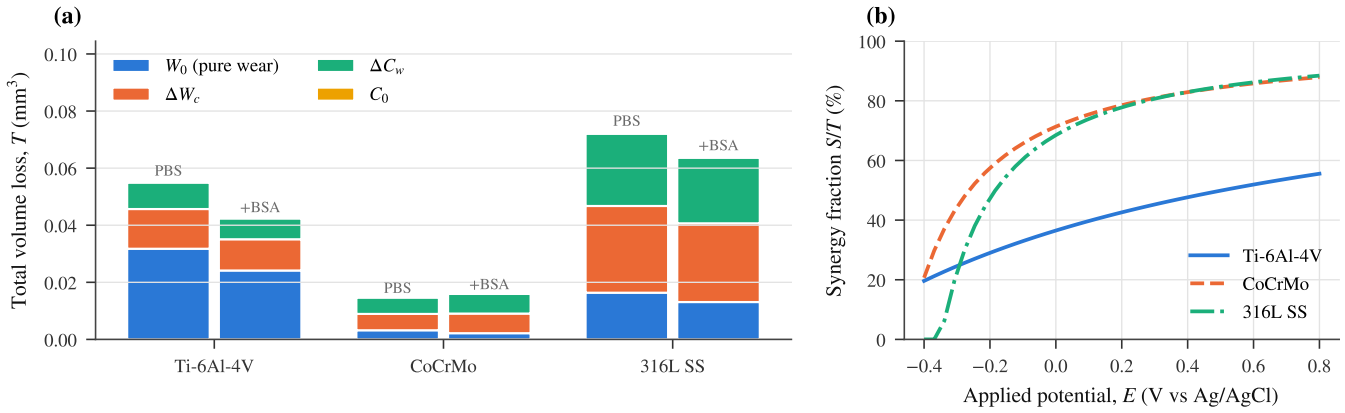

Fig. 6. (a) ASTM G119 decomposition of total loss in PBS and in PBS with 20 g L^{-1} BSA. (b) Synergy fraction versus applied potential (10 N, 1 Hz).

in the corrosion–wear regime on 66.3% and 61.2% of the area. No alloy reaches the corrosion-dominated regime at 10 N.

Velocity has a secondary effect. Because both the wear rate (4) and the number of depassivation events in (11) scale with f, Ψ is independent of velocity until t_ℓ approaches τ. Above about 100 mm s^{-1} ($f > 10$ Hz), incomplete repassivation bends the boundaries upward for CoCrMo and 316L. Load has a weak effect. From 1 to 40 N at $+0.2$ V, Ψ falls from 0.85 to 0.58 for Ti-6Al-4V, from 4.37 to 2.60 for CoCrMo and from 4.31 to 2.35 for 316L, without leaving the respective regime, because A_d and W_0 both grow nearly in proportion to F_n. The regime of a passive alloy is therefore set mainly by potential and repassivation kinetics, not by mechanical severity, within the Archard–asperity framework.

Fig. 8 complements the maps in load–potential space. The colour shows the chemical share $(C_0 + \Delta C_w)/T$, and the black contours show the total loss T. Below E_{pp}, the loss is purely mechanical and the contours are vertical. Above E_{pp}, they bend towards lower load, so the same total loss is reached at a lower load when the potential is high. For CoCrMo, a total loss of 0.01 mm^3 is reached at 4.1 N at $+0.6$ V but requires 26 N at -0.4 V.

F. Effect of Protein

Fig. 9 shows the effect of albumin concentration. Coverage saturates above about 15 g L^{-1} ($\theta_p = 0.75$ at 15 g L^{-1}). At 40 g L^{-1}, T decreases to 0.75 and 0.87 of its protein-free value for Ti-6Al-4V and 316L, and it increases to 1.10 for CoCrMo. The CoCrMo dissolved mass rises by 22%. This sign difference reproduces, by construction through η_c, the qualitative contrast between titanium and CoCrMo reported in serum tests [31]–[33]. The model adds a quantitative statement: the CoCrMo penalty saturates, so physiological protein levels (20–40 g L^{-1}) differ little from each other.

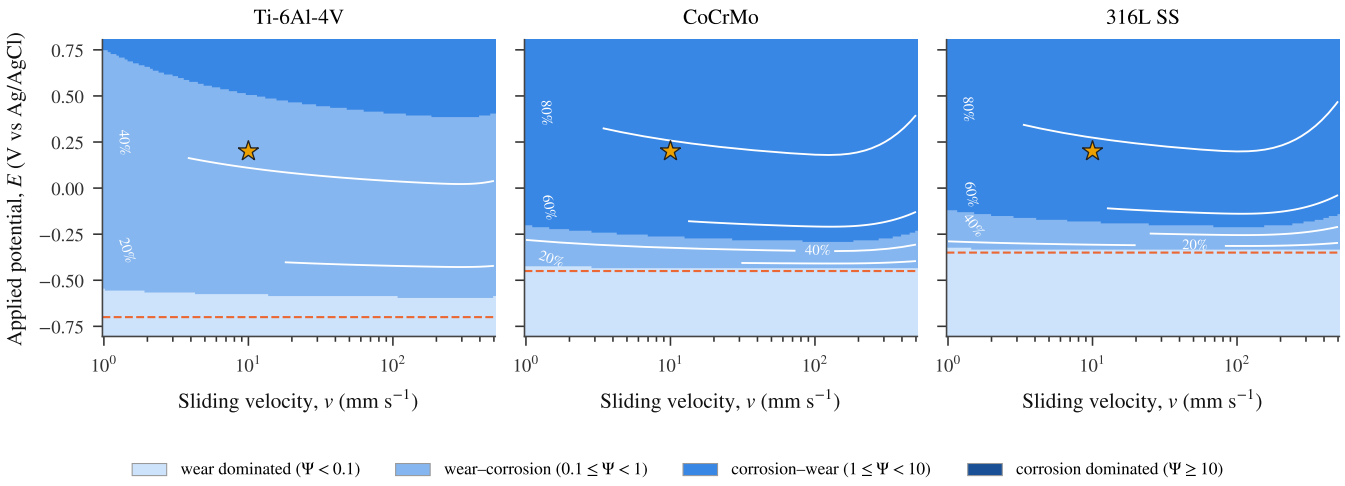

Fig. 7. Tribocorrosion mechanism maps in potential–velocity space ($F_n = 10$ N, 1 h, PBS) based on the corrosion-attribution ratio Ψ. White lines: iso-lines of synergy fraction S/T. Dashed line: E_{pp}. Star: reference condition.

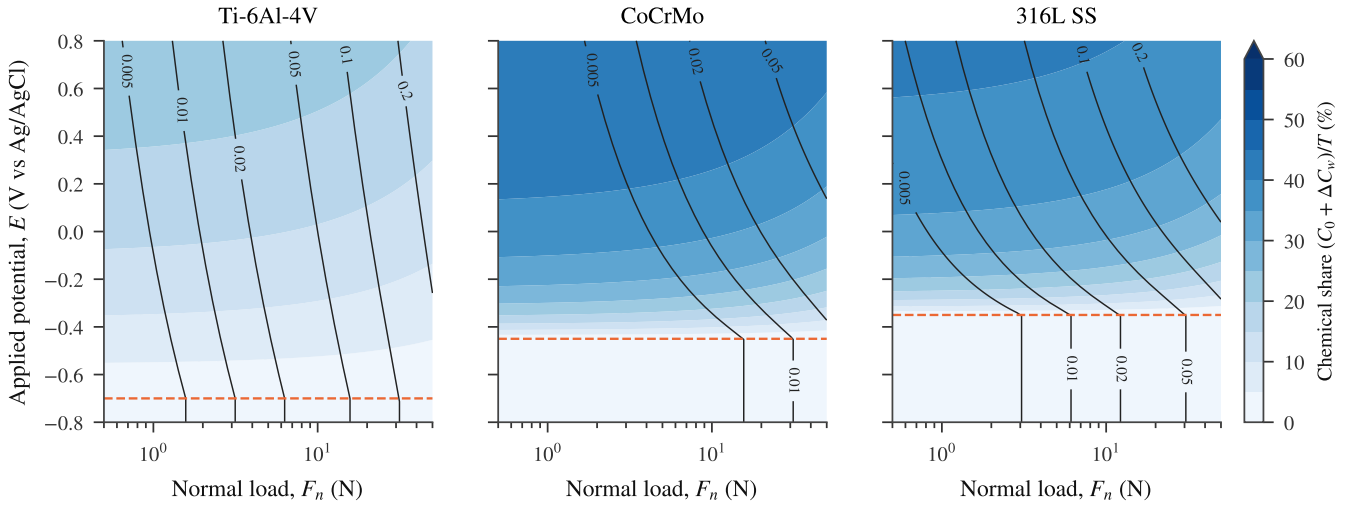

Fig. 8. Load–potential maps (1 Hz, 1 h, PBS). Colour: chemical share of the total loss. Black contours: total loss T (mm^3). Dashed line: E_{pp}.

G. Global Sensitivity Analysis

Table V and Fig. 10 give the Sobol indices for Ti-6Al-4V. For $\log_{10} T$, the most influential inputs are load ($S_T = 0.338$), frequency (0.176), the repassivation pair i_{pk} and τ (0.140 each), the wear coefficient (0.110) and the asperity radius (0.090). For dissolved metal, the repassivation pair dominates (0.268 each, 54% together), followed by the asperity radius (0.168) and load (0.151). The wear coefficient, hardness and third-body factor have almost no influence on dissolution. The potential matters only moderately (0.044) within $[-0.2, 0.6]$ V, because this window lies well above E_{pp} for Ti-6Al-4V. The sums of the first-order indices are 0.948 and 0.998, so the log outputs are nearly additive and interactions are weak; the gap between S_i and $S_{T,i}$ is largest for i_{pk} and τ in $\log_{10} T$, through the coupling between dissolution and third-body wear.

For experimentalists, two conclusions follow. First, measuring i_{pk} and τ, for instance by scratch or single-asperity repassivation tests, reduces the prediction uncertainty of ion release more than any other single measurement. Second, r_a, the micro-geometry of the contact, deserves to be characterised and reported, because it is the third

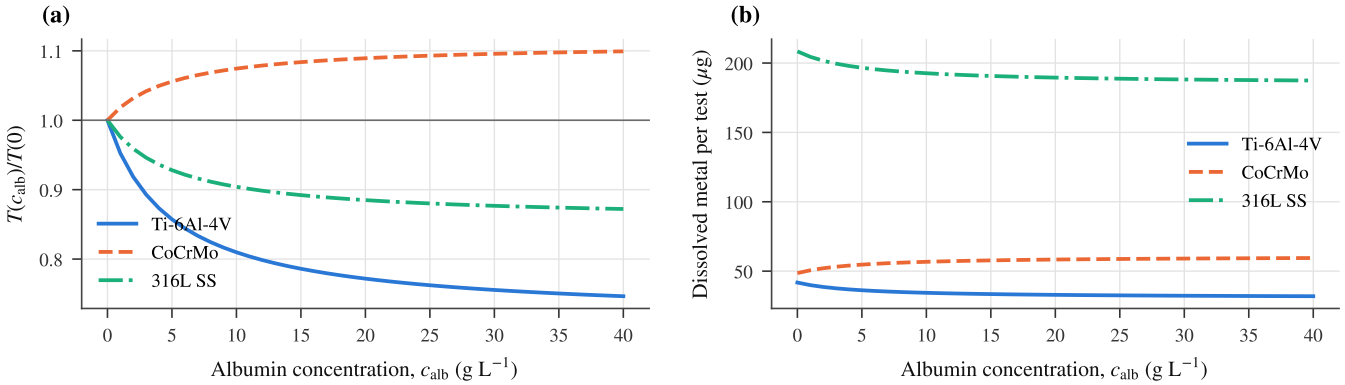

Fig. 9. Effect of albumin concentration (10 N, 1 Hz, +0.2 V, 1 h). (a) Total loss relative to PBS. (b) Dissolved metal per test.

most influential input yet it is rarely documented.

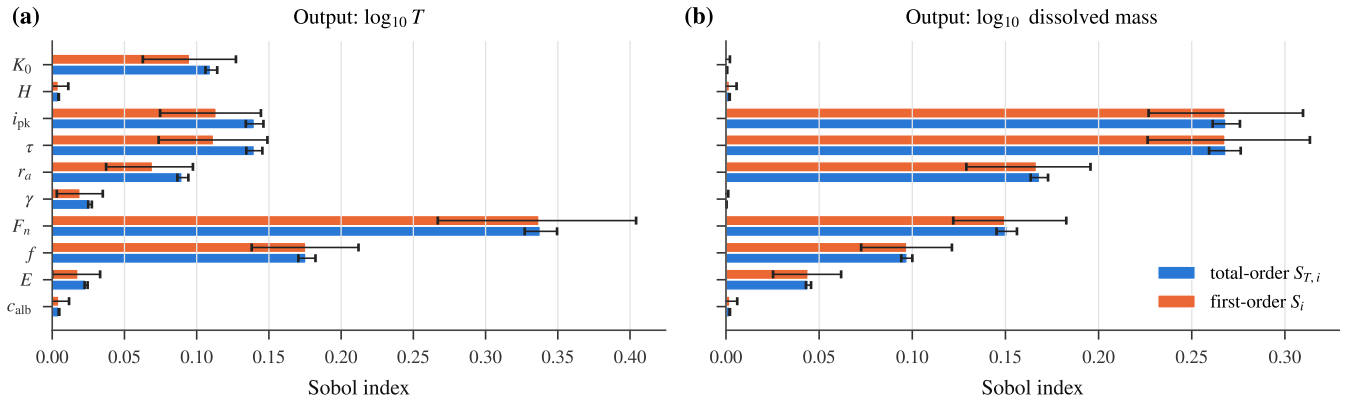

Fig. 10. First- and total-order Sobol indices for Ti-6Al-4V with 95% bootstrap intervals. (a) Output $\log_{10} T$. (b) Output $\log_{10}$ dissolved metal mass.

TABLE V
SOBOL INDICES FOR TI-6AL-4V ($N = 8192$, 98 304 MODEL RUNS)

	$\log_{10} T$		$\log_{10} m_{\text{ion}}$	
Input	S_i	$S_{T,i}$	S_i	$S_{T,i}$
K_0	0.095	0.110	0.000	0.001
H	0.004	0.004	0.002	0.002
i_{pk}	0.114	0.140	0.268	0.268
τ	0.112	0.140	0.268	0.268
r_a	0.069	0.090	0.167	0.168
γ	0.019	0.026	0.000	0.000
F_n	0.337	0.338	0.150	0.151
f	0.176	0.176	0.097	0.097
E	0.018	0.023	0.044	0.044
c_{alb}	0.005	0.005	0.002	0.002
$\sum$	0.948	1.052	0.998	1.002

H. Uncertainty Propagation

Fig. 11 and Table VI show the Monte Carlo results. The 90% interval of T spans a factor of 4.2 for Ti-6Al-4V and a factor of 6.3 for 316L. For dissolved metal, it spans a factor of about 9.7 for all three alloys. Parameter uncertainty alone therefore produces about one order of magnitude of scatter in ion release, which is comparable with the scatter often seen between laboratories. The ranking of total loss (CoCrMo $<$ Ti-6Al-4V $<$ 316L) is robust; the ranking of ion release between Ti-6Al-4V and CoCrMo is not, because their distributions overlap almost completely [Fig. 11(b)]. The regime classification is probabilistic too. Ti-6Al-4V is in the wear–corrosion regime with probability 62.7% and in the corrosion–wear regime with 36.5%, whereas CoCrMo and 316L are in the corrosion–wear regime with probabilities of 82.0% and 82.5%.

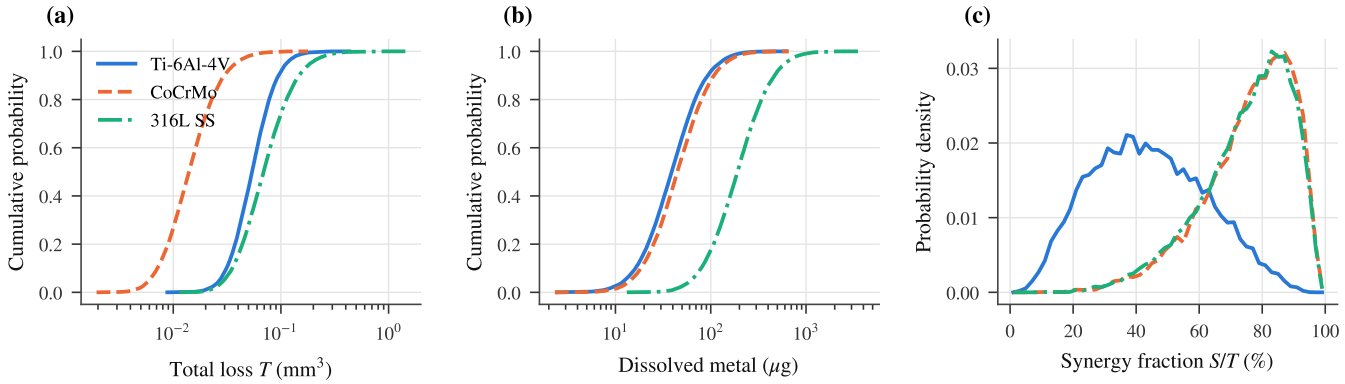

Fig. 11. Monte Carlo uncertainty propagation (2×10^4 samples per alloy) at the reference condition. Cumulative distributions of (a) total loss and (b) dissolved metal; (c) distribution of the synergy fraction.

TABLE VI
MONTE CARLO STATISTICS AT THE REFERENCE CONDITION

Quantity	Ti-6Al-4V	CoCrMo	316L SS
T median (mm^3)	0.0539	0.0140	0.0690
T 90% interval	0.0269–0.1127	0.0060–0.0380	0.0295–0.1873
m_{ion} median (μg)	38.7	44.6	190.7
m_{ion} 90% interval	12.6–121.8	14.4–140.0	62.2–603.7
S/T median (%)	43.0	78.5	77.8
P(wear dominated) (%)	0.7	0.0	0.0
P(wear–corrosion) (%)	62.7	5.9	6.7
P(corrosion–wear) (%)	36.5	82.0	82.5
P(corrosion dominated) (%)	0.1	12.1	10.8

I. Surface-Engineering Design Map

Surface treatments act on two levers in the model: hardness, through $h = H_s/H$, and the depassivation charge, through a multiplier ϕ_q on i_{pk} that represents a thicker or more protective oxide or coating. We assume, in addition, that harder layers reduce the wear coefficient as $K_0 h^{-1/2}$. Fig. 12 maps the resulting reduction of T for Ti-6Al-4V. The contours are nearly vertical at small ϕ_q and nearly horizontal at small h, so the two levers are complementary: once either term is small, improving it further brings little.

Table VII evaluates four treatment families placed on the map with illustrative (h, ϕ_q) values. These positions are assumptions chosen to represent typical behaviour, not measured properties of specific processes. Plasma nitriding ($h = 4$, $\phi_q = 0.3$) reduces T by 89%. Thermal oxidation ($h = 2.5$, $\phi_q = 0.15$) gives an 83% reduction with a lower synergy fraction (15.7%), consistent with the reported benefit of thermally grown rutile in fretting corrosion [41]. Anodic TiO_2 nanotubes, which change hardness little ($h = 1.3$), reduce T by 48%; their main benefit is biological

[42]. A DLC-type coating ($h = 6$, $\phi_q = 0.05$) gives 96%, under the strong assumption that the coating stays intact [17].

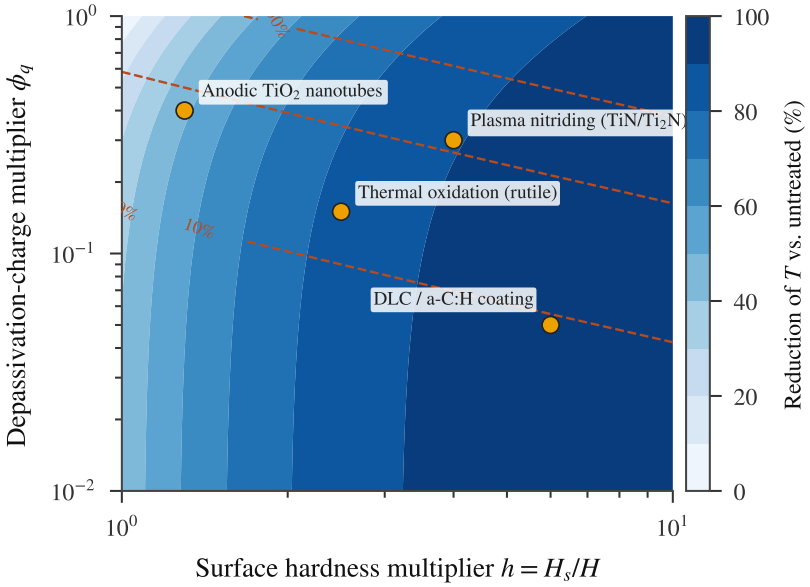

Fig. 12. Design map for Ti-6Al-4V (10 N, 1 Hz, +0.2 V, 1 h): reduction of total loss versus hardness multiplier h and depassivation-charge multiplier ϕ_q. Dashed lines: iso-lines of S/T (10%, 30%, 50%). Markers: illustrative treatment positions.

TABLE VII
PREDICTED EFFECT OF ILLUSTRATIVE SURFACE TREATMENTS ON TI-6AL-4V (CLOSED FORM; TREATMENT POSITIONS (h, ϕ_q) ARE ASSUMPTIONS)

Treatment (illustrative)	h	ϕ_q	T (10^{-3} mm^3)	ΔT (%)	m_{ion} (μg)	S/T (%)
Untreated Ti-6Al-4V	1.0	1.00	55.34	0.0	41.8	42.6
Plasma nitriding (TiN/Ti_2N)	4.0	0.30	5.89	89.4	3.4	32.6
Thermal oxidation (rutile)	2.5	0.15	9.53	82.8	2.6	15.7
Anodic TiO_2 nanotubes	1.3	0.40	28.77	48.0	13.0	25.5
DLC / a-C:H coating	6.0	0.05	2.38	95.7	0.4	9.1

J. Fretting Corrosion at a Ceramic-Head Modular Taper

Fig. 13 and Table VIII show the fretting projection. The micro-contact gross-slip thresholds δ_t are 0.15, 0.13 and 0.07 μm. Measured taper micromotions of a few micrometres therefore place every asperity in gross slip, and partial slip matters only for sub-micrometre motion. With a fixed potential, the dissolved mass would rise steeply with amplitude [thin lines in Fig. 13(a)]. With OCP coupling, the dissolved mass flattens to 17.5, 10.8 and 22.1 mg per 10^6 cycles at 5 μm, which is 2.7–6.6 times below the fixed-potential bound. The taper potential falls with amplitude [Fig. 13(b)], to -0.48 V for Ti-6Al-4V at 5 μm and -0.62 V at 20 μm. Under these assumptions, the release at a taper is controlled by the cathodic capacity of the surrounding passive surface ($A_{\mathrm{cath}}\, i_{\mathrm{lim}}$), rather than by the micromotion amplitude.

This finding has two practical implications. First, reducing micromotion beyond the gross-slip threshold may not reduce ion release proportionally, while reducing the oxygen supply or the cathodic area (for instance through coatings on the exposed stem) might. Second, the absolute numbers depend on A_{cath}, i_{lim} and the crevice chemistry. They should be read as an order-of-magnitude upper estimate under bulk-electrolyte assumptions; crevice acidification and oxygen depletion are not modelled [12], [27], [28].

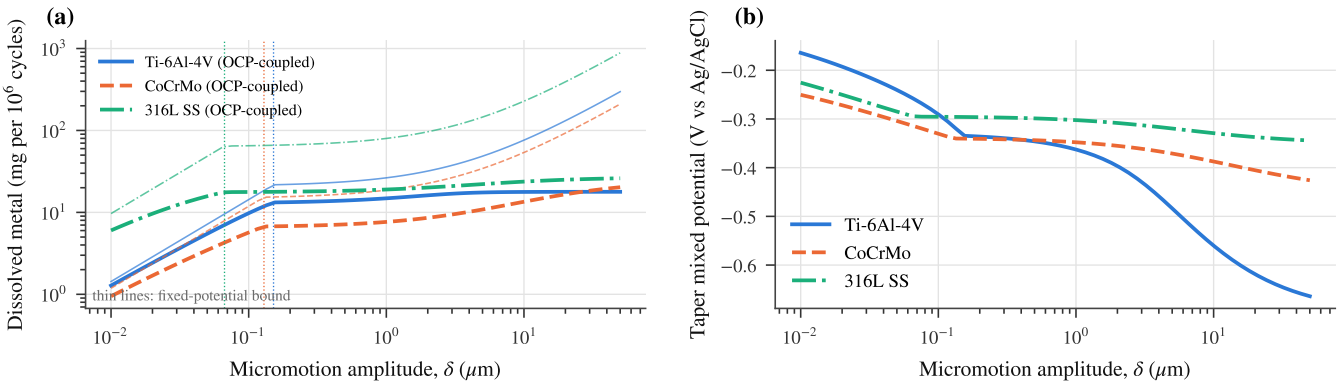

Fig. 13. Fretting projection for a ceramic-head modular taper ($A_t = 150$ mm^2, $p_n = 50$ MPa, 1 Hz). (a) Dissolved metal per 10^6 cycles, OCP-coupled (thick) and fixed-potential bound (thin); dotted lines mark δ_t. (b) Mixed potential of the taper.

TABLE VIII
FRETTING PROJECTION AT $\delta = 5$ μM (DISSOLVED METAL PER 10^6 CYCLES)

Alloy	δ_t (μm)	E_{mix} at 5 μm (V)	OCP-coupled (mg)	Fixed-E bound (mg)
Ti-6Al-4V	0.15	-0.483	17.491	48.33
CoCrMo	0.13	-0.371	10.826	34.19
316L SS	0.07	-0.320	22.111	145.05

VI. DISCUSSION

A. What the Model Explains

Three widely reported experimental observations emerge from the model without being imposed. First, the OCP drops on sliding and saturates with load [Fig. 5(b)], as in OCP tribocorrosion tests [6], [7]. Second, the anodic current grows sub-linearly with load [Fig. 5(a)]. Mischler's model predicts an exponent of about 0.5 for plastic asperity contact [7]; our exponent of 0.82–0.88 comes from the asperity sweep with saturation and track widening, and the difference is a testable discriminator between the two descriptions. Third, the synergy fraction increases with potential [Fig. 6(b)], as reported for passive alloys under potentiostatic control [6], [30], [37].

The model also yields less obvious insights. The tribocorrosion regime is governed by potential and repassivation kinetics rather than by load. A large OCP drop does not imply a large synergy. Volume loss and ion release can rank alloys differently. Taper release can be capped by the cathode. Each is a hypothesis that can be tested with existing apparatus.

B. Relation to Experimental Practice

ASTM G119 requires separate tests for W_0 (under cathodic protection) and C_0 (static corrosion) [9]. In the model, these are obtained from the same run, so the decomposition is free of the specimen-to-specimen scatter that complicates experimental synergy estimates [8], [19]. Conversely, the model needs experimental input, chiefly i_{pk}, τ and r_a, the parameters ranked highest by the sensitivity analysis. A practical calibration path is to measure the repassivation transient in a single-scratch test, the wear coefficient under cathodic protection, and r_a from profilometry of the counterbody, and then to predict the full G119 decomposition at other conditions.

C. Limitations

The framework has several limitations. (i) All parameters are representative values from published ranges; no experimental data were fitted, and the absolute numbers carry the uncertainties shown in Table VI. (ii) Archard's law with a constant coefficient ignores running-in, tribofilm formation and the graphitic or protein-derived layers reported for CoCrMo [34]–[36]. (iii) The protein model is a Langmuir surrogate with signed efficiencies; protein

denaturation, competitive adsorption and complexation chemistry are not resolved [31], [32]. (iv) The third-body term is linear in the dissolution rate, whereas debris retention depends on contact geometry and lubrication [21]. (v) The potential distribution in the electrolyte is not resolved, so ohmic drop and current distribution effects modelled by Papageorgiou and Mischler [24] are absent. (vi) The averaged current loses accuracy when $\tau/t_\ell > 0.05$ (Fig. 2). (vii) The fretting model omits crevice acidification, oxygen depletion and the elastic compliance of the taper [12], [28]. These limits define the next steps: calibration and validation against new potentiostatic and OCP experiments on all three alloys, and coupling with a finite-element potential solver.

VII. Conclusion

We presented TriboSyn, a physics-based framework that predicts the ASTM G119 decomposition, the OCP and metal release of passive biomedical alloys from contact mechanics and repassivation kinetics, and that quantifies which inputs control those predictions. The averaged model was verified against a pass-resolved simulation (0.29% error at 1 Hz) and its closed form against an adaptive ODE solution (1.37% mean error). At 10 N, 1 Hz and $+0.2$ V in PBS, the predicted synergy fractions were 42.2%, 78.2% and 77.3% for Ti-6Al-4V, CoCrMo and 316L. The corrosion–wear boundary lay at $+0.51$, -0.26 and -0.18 V, and albumin raised CoCrMo ion release by about 20% while it lowered the Ti-6Al-4V loss. The repassivation parameters i_{pk} and τ explained 54% of the variance in dissolved metal, and parameter uncertainty produced about one order of magnitude of spread in ion release. Surface treatments that combine hardening with a lower depassivation charge were predicted to reduce total loss by more than 80%. At a modular taper, metal release was capped by the cathodic capacity rather than by the micromotion amplitude. These predictions are hypotheses for targeted experiments, and the framework is intended to be calibrated against them.

Declarations

Funding: The authors received no specific funding for this research from any funding agency in the public, commercial, or not-for-profit sectors.

Data Availability: The data supporting the findings of this study are available from the corresponding author upon reasonable request.

Competing Interests: The authors declare that they have no competing interests that could have influenced the work reported in this manuscript.

Ethical Statement: Not applicable; the study involved no human participants, animals or personal data.

References

[1] M. Geetha, A. K. Singh, R. Asokamani, and A. K. Gogia, "Ti based biomaterials, the ultimate choice for orthopaedic implants – a review," *Prog. Mater. Sci.*, vol. 54, no. 3, pp. 397–425, 2009, doi: 10.1016/j.pmatsci.2008.06.004.

[2] M. Long and H. J. Rack, "Titanium alloys in total joint replacement—a materials science perspective," *Biomaterials*, vol. 19, no. 18, pp. 1621–1639, 1998, doi: 10.1016/S0142-9612(97)00146-4.

[3] Q. Chen and G. A. Thouas, "Metallic implant biomaterials," *Mater. Sci. Eng. R*, vol. 87, pp. 1–57, 2015, doi: 10.1016/j.mser.2014.10.001.

[4] M. Niinomi, "Mechanical properties of biomedical titanium alloys," *Mater. Sci. Eng. A*, vol. 243, no. 1–2, pp. 231–236, 1998, doi: 10.1016/S0921-5093(97)00806-X.

[5] D. Landolt, "Electrochemical and materials aspects of tribocorrosion systems," *J. Phys. D: Appl. Phys.*, vol. 39, no. 15, pp. 3121–3127, 2006, doi: 10.1088/0022-3727/39/15/S01.

[6] D. Landolt, S. Mischler, and M. Stemp, "Electrochemical methods in tribocorrosion: A critical appraisal," *Electrochim. Acta*, vol. 46, no. 24–25, pp. 3913–3929, 2001, doi: 10.1016/S0013-4686(01)00679-X.

[7] S. Mischler, "Triboelectrochemical techniques and interpretation methods in tribocorrosion: A comparative evaluation," *Tribol. Int.*, vol. 41, no. 7, pp. 573–583, 2008, doi: 10.1016/j.triboint.2007.11.003.

[8] S. W. Watson, F. J. Friedersdorf, B. W. Madsen, and S. D. Cramer, "Methods of measuring wear-corrosion synergism," *Wear*, vol. 181–183, pp. 476–484, 1995, doi: 10.1016/0043-1648(95)90161-2.

[9] ASTM International, "Standard guide for determining synergism between wear and corrosion," ASTM G119-09(2021), West Conshohocken, PA, USA, 2021, doi: 10.1520/G0119-09R21.

[10] M. T. Mathew, P. S. Pai, R. Pourzal, A. Fischer, and M. A. Wimmer, "Significance of tribocorrosion in biomedical applications: Overview and current status," *Adv. Tribol.*, vol. 2009, p. 250986, 2009, doi: 10.1155/2009/250986.

[11] J. J. Jacobs, J. L. Gilbert, and R. M. Urban, "Corrosion of metal orthopaedic implants," *J. Bone Joint Surg. Am.*, vol. 80, no. 2, pp. 268–282, 1998, doi: 10.2106/00004623-199802000-00015.

[12] J. L. Gilbert, C. A. Buckley, and J. J. Jacobs, "In vivo corrosion of modular hip prosthesis components in mixed and similar metal combinations. The effect of crevice, stress, motion, and alloy coupling," *J. Biomed. Mater. Res.*, vol. 27, no. 12, pp. 1533–1544, 1993, doi: 10.1002/jbm.820271210.

[13] H. J. Cooper, C. J. D. Valle, R. A. Berger, M. Tetreault, W. G. Paprosky, S. M. Sporer, and J. J. Jacobs, "Corrosion at the head-neck taper as a cause for adverse local tissue reactions after total hip arthroplasty," *J. Bone Joint Surg. Am.*, vol. 94, no. 18, pp. 1655–1661, 2012, doi: 10.2106/JBJS.K.01352.

[14] J. Villanueva, L. Trino, J. Thomas, L. Mercuri, M. M. Stack, and M. T. Mathew, "Corrosion, tribology, and tribocorrosion research in biomedical implants: Progressive trend in the published literature," *J. Bio- Tribo-Corros.*, 2017, doi: 10.1007/s40735-016-0060-1.

[15] C. D. d. R. Barros, J. C. Rocha, I. N. Bastos, and J. A. C. P. Gomes, "Tribocorrosion resistance of dental implant alloys—assessment of cp-Ti, Ti6Al4V, and NiCr in neutral and acidified saliva," *J. Bio- Tribo-Corros.*, vol. 7, no. 2, p. 73, 2021, doi: 10.1007/s40735-021-00508-5.

[16] C. B. von der Ohe, R. Johnsen, and N. Espallargas, "Modeling the multi-degradation mechanisms of combined tribocorrosion interacting with static and cyclic loaded surfaces of passive metals exposed to seawater," *Wear*, vol. 269, no. 7–8, pp. 607–616, 2010, doi: 10.1016/j.wear.2010.06.010.

[17] R. J. K. Wood, "Tribo-corrosion of coatings: A review," *J. Phys. D: Appl. Phys.*, vol. 40, no. 18, pp. 5502–5521, 2007, doi: 10.1088/0022-3727/40/18/S10.

[18] K. Holmberg and A. Erdemir, "Influence of tribology on global energy consumption, costs and emissions," *Friction*, vol. 5, no. 3, pp. 263–284, 2017, doi: 10.1007/s40544-017-0183-5.

[19] A. López-Ortega, J. L. Arana, and R. Bayón, "Tribocorrosion of passive materials: A review on test procedures and standards," *Int. J. Corros.*, vol. 2018, p. 7345346, 2018, doi: 10.1155/2018/7345346.

[20] P. Jemmely, S. Mischler, and D. Landolt, "Electrochemical modeling of passivation phenomena in tribocorrosion," *Wear*, vol. 237, no. 1, pp. 63–76, 2000, doi: 10.1016/S0043-1648(99)00314-2.

[21] D. Landolt, S. Mischler, M. Stemp, and S. Barril, "Third body effects and material fluxes in tribocorrosion systems involving a sliding contact," *Wear*, vol. 256, no. 5, pp. 517–524, 2004, doi: 10.1016/S0043-1648(03)00561-1.

[22] S. Cao, S. G. Maldonado, and S. Mischler, "Tribocorrosion of passive metals in the mixed lubrication regime: Theoretical model and application to metal-on-metal artificial hip joints," *Wear*, vol. 324–325, pp. 55–63, 2015, doi: 10.1016/j.wear.2014.12.003.

[23] S. Cao and S. Mischler, "Modeling tribocorrosion of passive metals – a review," *Curr. Opin. Solid State Mater. Sci.*, vol. 22, no. 4, pp. 127–141, 2018, doi: 10.1016/j.cossms.2018.06.001.

[24] N. Papageorgiou and S. Mischler, "Electrochemical simulation of the current and potential response in sliding tribocorrosion," *Tribol. Lett.*, vol. 48, no. 3, pp. 271–283, 2012, doi: 10.1007/s11249-012-0022-9.

[25] M. M. Stack and K. Chi, "Mapping sliding wear of steels in aqueous conditions," *Wear*, vol. 255, no. 1–6, pp. 456–465, 2003, doi: 10.1016/S0043-1648(03)00203-5.

[26] S. C. Lim and M. F. Ashby, "Overview no. 55 wear-mechanism maps," *Acta Metall.*, vol. 35, no. 1, pp. 1–24, 1987, doi: 10.1016/0001-6160(87)90209-4.

[27] A. Mace and J. L. Gilbert, "Micro asperity-based fretting corrosion of CoCrMo, Ti-6Al-4V, and 316L SS: Assessment of an electrochemical and micro-mechanical model," *Tribol. Int.*, vol. 180, p. 108222, 2023, doi: 10.1016/j.triboint.2023.108222.

[28] V. Swaminathan and J. L. Gilbert, "Fretting corrosion of CoCrMo and Ti6Al4V interfaces," *Biomaterials*, vol. 33, no. 22, pp. 5487–5503, 2012, doi: 10.1016/j.biomaterials.2012.04.015.

[29] S. Barril, S. Mischler, and D. Landolt, "Influence of fretting regimes on the tribocorrosion behaviour of Ti6Al4V in 0.9 wt.% sodium chloride solution," *Wear*, vol. 256, no. 9–10, pp. 963–972, 2004, doi: 10.1016/j.wear.2003.09.005.

[30] Y. Yan, A. Neville, D. Dowson, and S. Williams, "Tribocorrosion in implants—assessing high carbon and low carbon Co–Cr–Mo alloys by in situ electrochemical measurements," *Tribol. Int.*, vol. 39, no. 12, pp. 1509–1517, 2006, doi: 10.1016/j.triboint.2006.01.016.

[31] Y. Yan, A. Neville, and D. Dowson, "Biotribocorrosion of CoCrMo orthopaedic implant materials—assessing the formation and effect of the biofilm," *Tribol. Int.*, vol. 40, no. 10–12, pp. 1492–1499, 2007, doi: 10.1016/j.triboint.2007.02.019.

[32] F. Contu, B. Elsener, and H. Böhni, "Corrosion behaviour of CoCrMo implant alloy during fretting in bovine serum," *Corros. Sci.*, vol. 47, pp. 1863–1875, 2005, doi: 10.1016/j.corsci.2004.09.003.

[33] S. Mischler and A. I. Muñoz, "Wear of CoCrMo alloys used in metal-on-metal hip joints: A tribocorrosion appraisal," *Wear*, vol. 297, no. 1–2, pp. 1081–1094, 2013, doi: 10.1016/j.wear.2012.11.061.

[34] Y. Liao, R. Pourzal, M. A. Wimmer, J. J. Jacobs, A. Fischer, and L. D. Marks, "Graphitic tribological layers in metal-on-metal hip replacements," *Science*, vol. 334, no. 6063, pp. 1687–1690, 2011, doi: 10.1126/science.1213902.

[35] M. A. Wimmer, R. Nassutt, C. Sprecher, J. Loos, G. Täger, and A. Fischer, "Investigation on stick phenomena in metal-on-metal hip joints after resting periods," *Proc. Inst. Mech. Eng. H, J. Eng. Med.*, vol. 220, no. 2, pp. 219–227, 2006, doi: 10.1243/09544119JEIM117.

[36] W. Q. Toh, X. Tan, A. Bhowmik, E. Liu, and S. B. Tor, "Tribochemical characterization and tribocorrosive behavior of CoCrMo alloys: A review," *Materials*, vol. 11, no. 1, p. 30, 2018, doi: 10.3390/ma11010030.

[37] M. K. Dimah, F. D. Albeza, V. A. Borrás, and A. I. Muñoz, "Study of the biotribocorrosion behaviour of titanium biomedical alloys in simulated body fluids by electrochemical techniques," *Wear*, vol. 294–295, pp. 409–418, 2012, doi: 10.1016/j.wear.2012.04.014.

[38] M. P. Licausi, A. I. Muñoz, and V. A. Borrás, "Influence of the fabrication process and fluoride content on the tribocorrosion behaviour of Ti6Al4V biomedical alloy in artificial saliva," *J. Mech. Behav. Biomed. Mater.*, vol. 20, pp. 137–148, 2013, doi: 10.1016/j.jmbbm.2013.01.019.

[39] C. Dini, R. C. Costa, C. Sukotjo, C. G. Takoudis, M. T. Mathew, and V. A. R. Barão, "Progression of bio-tribocorrosion in implant dentistry," *Front. Mech. Eng.*, vol. 6, 2020, doi: 10.3389/fmech.2020.00001.

[40] J. Stendal, O. Fergani, H. Yamaguchi, and N. Espallargas, "A comparative tribocorrosion study of additive manufactured and wrought 316L stainless steel in simulated body fluids," *J. Bio- Tribo-Corros.*, 2018, doi: 10.1007/s40735-017-0125-9.

[41] S. Kumar, T. S. N. S. Narayanan, S. G. S. Raman, and S. K. Seshadri, "Surface modification of CP-Ti to improve the fretting-corrosion resistance: Thermal oxidation vs. anodizing," *Mater. Sci. Eng. C*, vol. 30, no. 6, pp. 921–927, 2010, doi: 10.1016/j.msec.2010.03.024.

[42] P. Roy, S. Berger, and P. Schmuki, "TiO_2 nanotubes: Synthesis and applications," *Angew. Chem. Int. Ed.*, vol. 50, no. 13, pp. 2904–2939, 2011, doi: 10.1002/anie.201001374.

[43] K. L. Johnson, *Contact Mechanics*. Cambridge, U.K.: Cambridge Univ. Press, 1985, doi: 10.1017/CBO9781139171731.

[44] J. F. Archard, "Contact and rubbing of flat surfaces," *J. Appl. Phys.*, vol. 24, no. 8, pp. 981–988, 1953, doi: 10.1063/1.1721448.

[45] I. M. Sobol', "Global sensitivity indices for nonlinear mathematical models and their Monte Carlo estimates," *Math. Comput. Simul.*, vol. 55, no. 1–3, pp. 271–280, 2001, doi: 10.1016/S0378-4754(00)00270-6.

[46] A. Saltelli, P. Annoni, I. Azzini, F. Campolongo, M. Ratto, and S. Tarantola, "Variance based sensitivity analysis of model output. Design and estimator for the total sensitivity index," *Comput. Phys. Commun.*, vol. 181, no. 2, pp. 259–270, 2010, doi: 10.1016/j.cpc.2009.09.018.